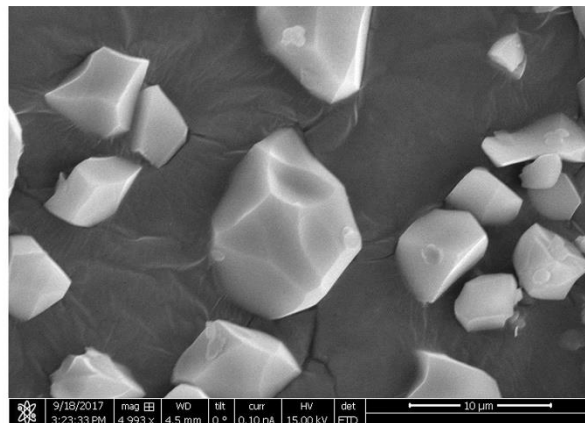
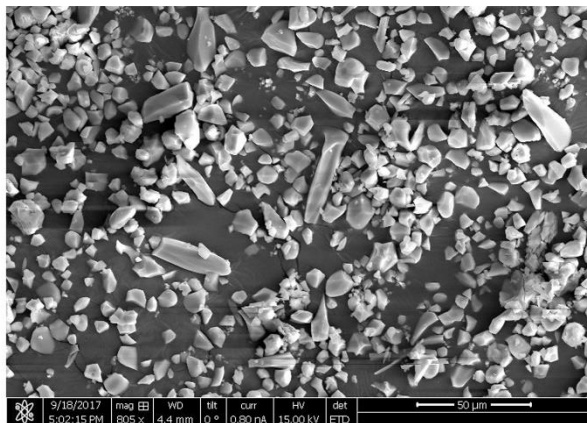


1  
2  
3  
4  
5  
6  
7  
8  
9  
10  
11  
12  
13  
14  
15  
16

# Supplementary Information

## A Robust Zirconium Amino Acid Metal-Organic Framework for Proton Conduction

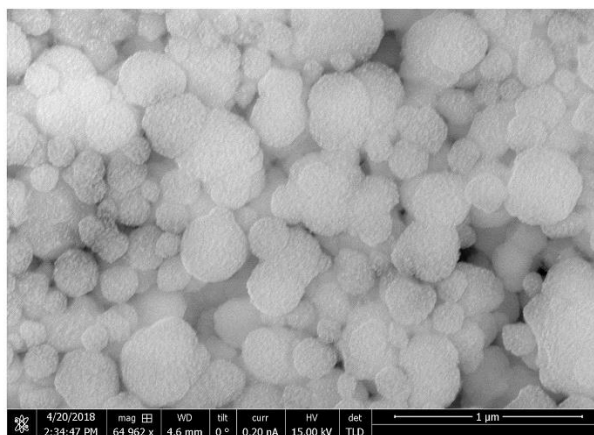
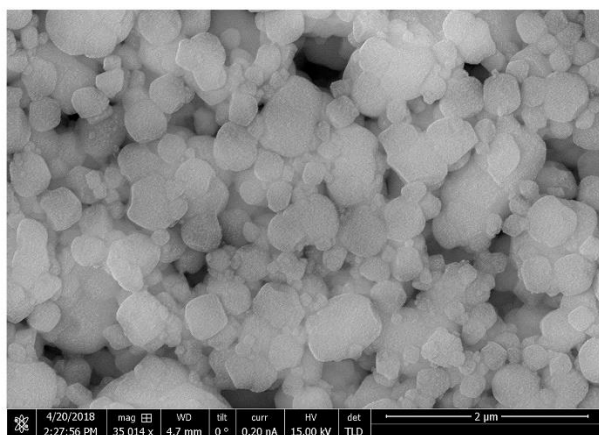
Sujing Wang et al.



17

18 **Supplementary Figure 1.** SEM images of MIP-202(Zr) sample with different magnifications obtained from  
19 reaction without stirring.

20



21

22 **Supplementary Figure 2.** SEM images of MIP-202(Zr) sample with different magnifications obtained from  
23 reaction with stirring.

24

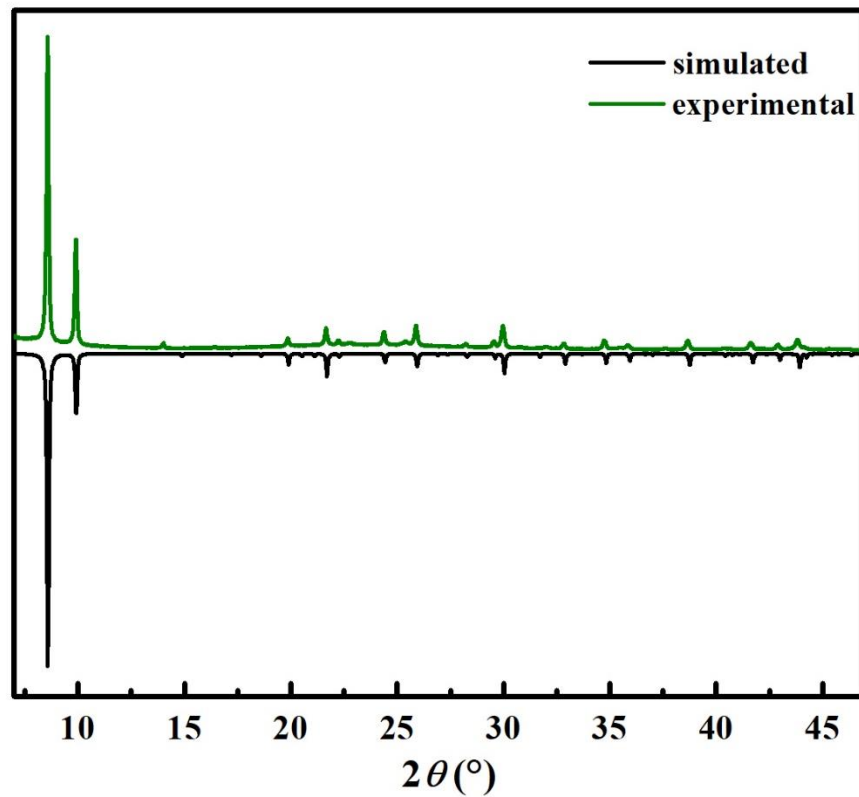
25

26

27

28

29



30

31 **Supplementary Figure 3** Comparison between the experimental PXRD pattern and the calculated data obtained

32 from the DFT optimized geometry of the MIP-202(Zr) solid.

33

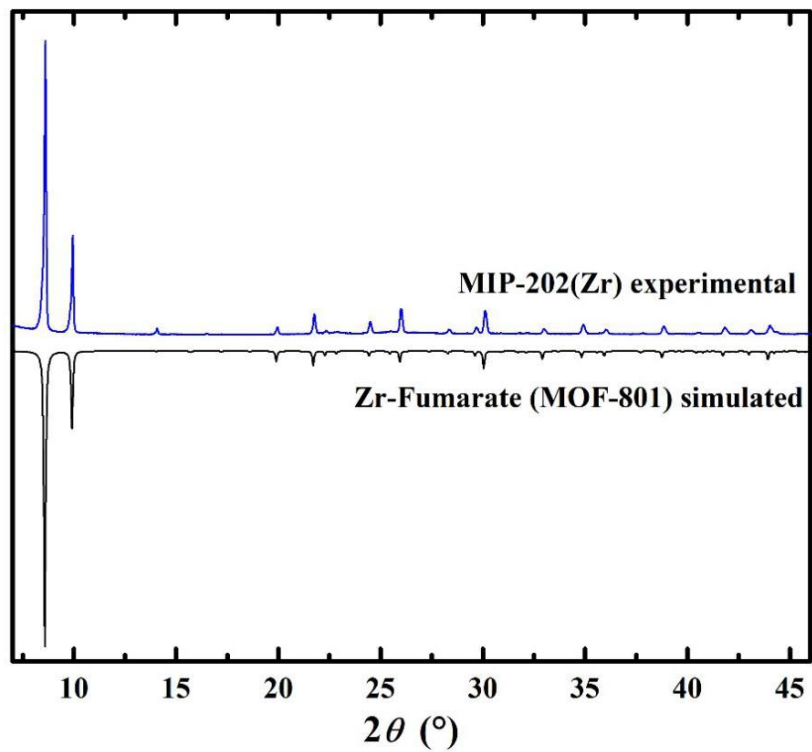
34

35

36

37

38



39

40 **Supplementary Figure 4.** PXRD pattern comparison of MIP-202(Zr) and Zr-Fumarate.

41

42

43

44

45

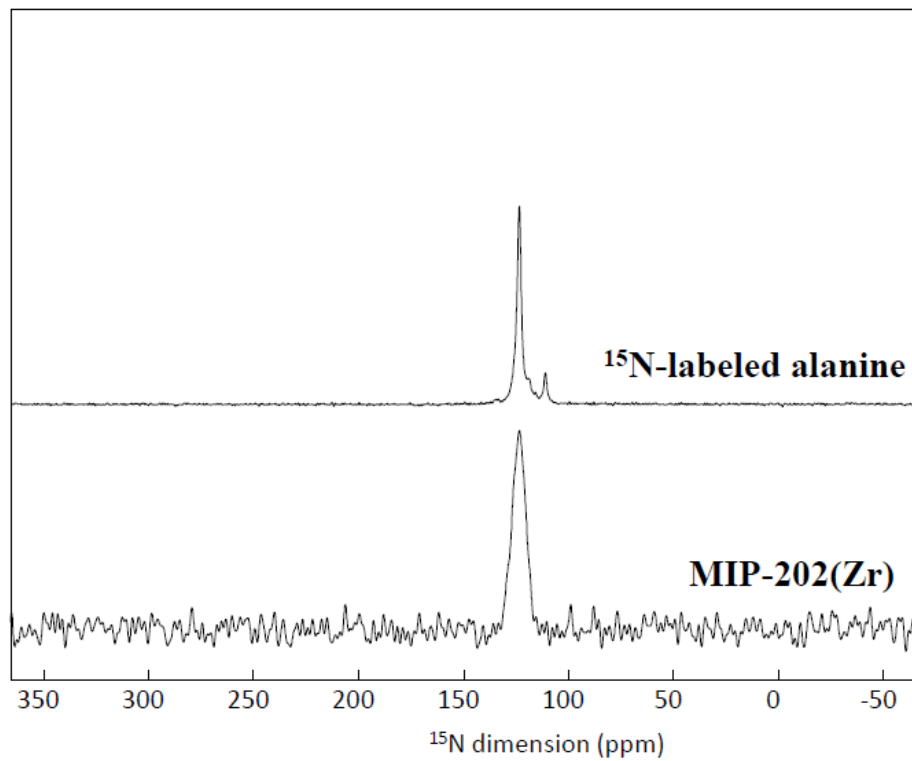
46

47

48

49

50



51

52 **Supplementary Figure 5.**  $^{15}\text{N}$  CPMAS (11.7 T, MAS 10 kHz) solid-state NMR spectra of MIP-202(Zr) ( $^{15}\text{N}$  natural  
53 abundance aspartic linker) compared to that of zwitterionic alanine ( $^{15}\text{N}$ - $^{13}\text{C}$  doubly-labeled compound).

54

55

56

57

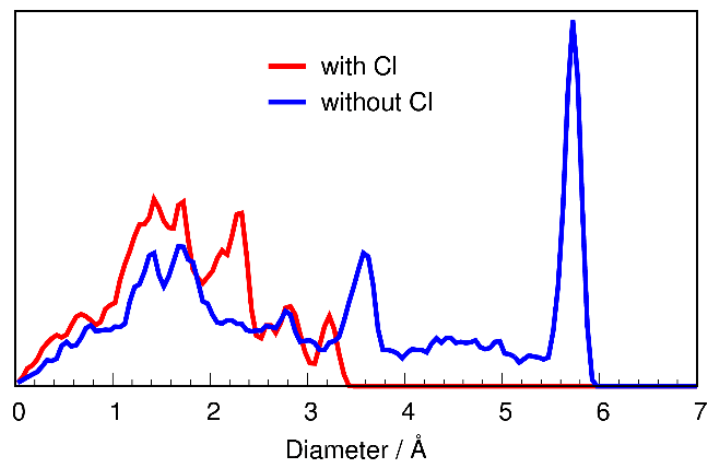
58

59

60

61

62



63

64 **Supplementary Figure 6.** Simulated Pore size distribution (PSD) of MIP-202(Zr) with and without the Cl<sup>-</sup> ions  
65 present in the pores obtained by applying the geometric method to the crystal structure

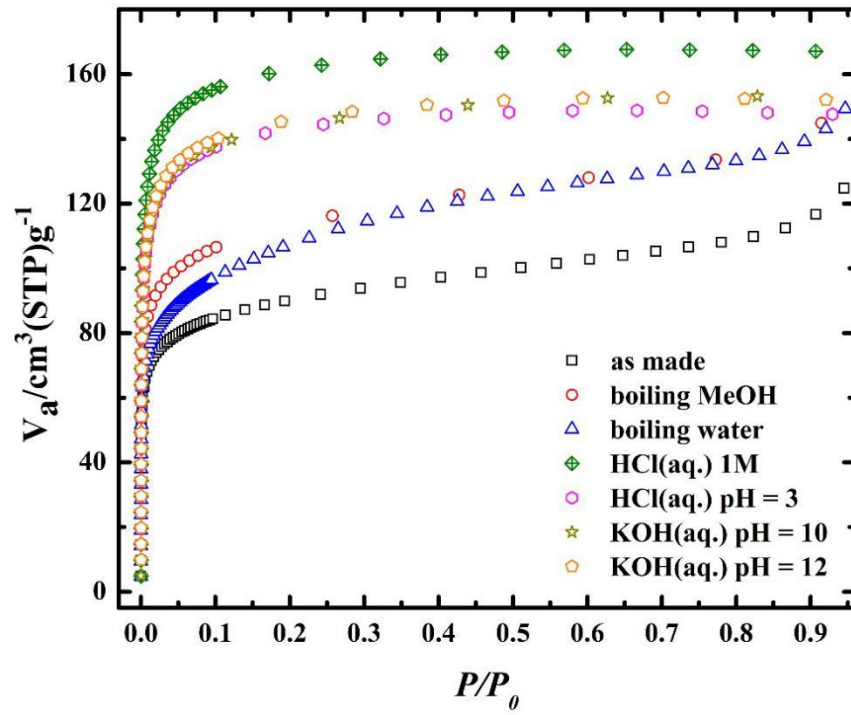
66

67

68

69

70



71

72 **Supplementary Figure 7.** Nitrogen adsorption isotherm comparison of MIP-202(Zr) samples before and after  
 73 various chemical treatments.

74

75

76

77

78

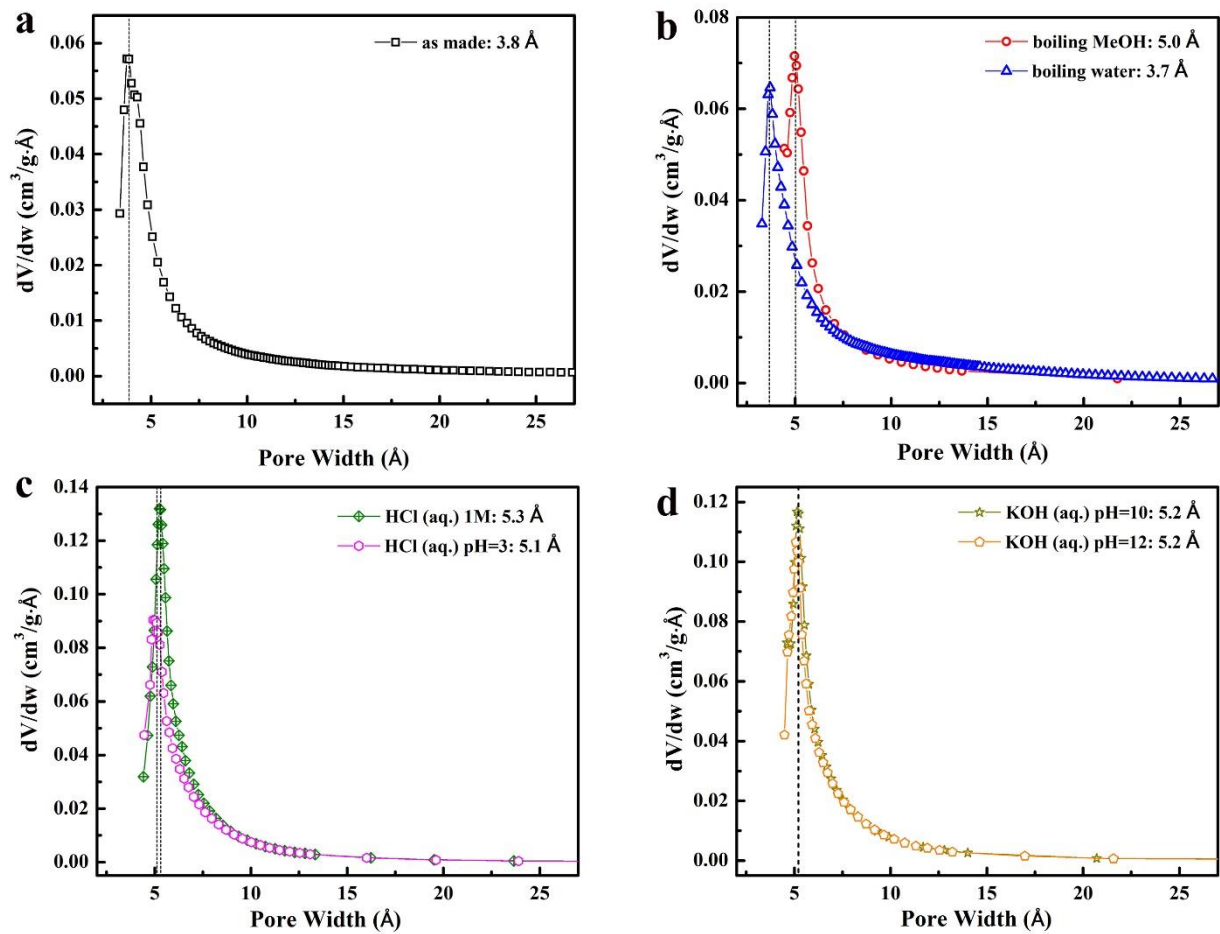
79

80

81

82

83



84

85 **Supplementary Figure 8.** Pore size distribution deduced from nitrogen adsorption isotherms for MIP-202(Zr)

86 samples before and after various chemical treatments.

87

88

89

90

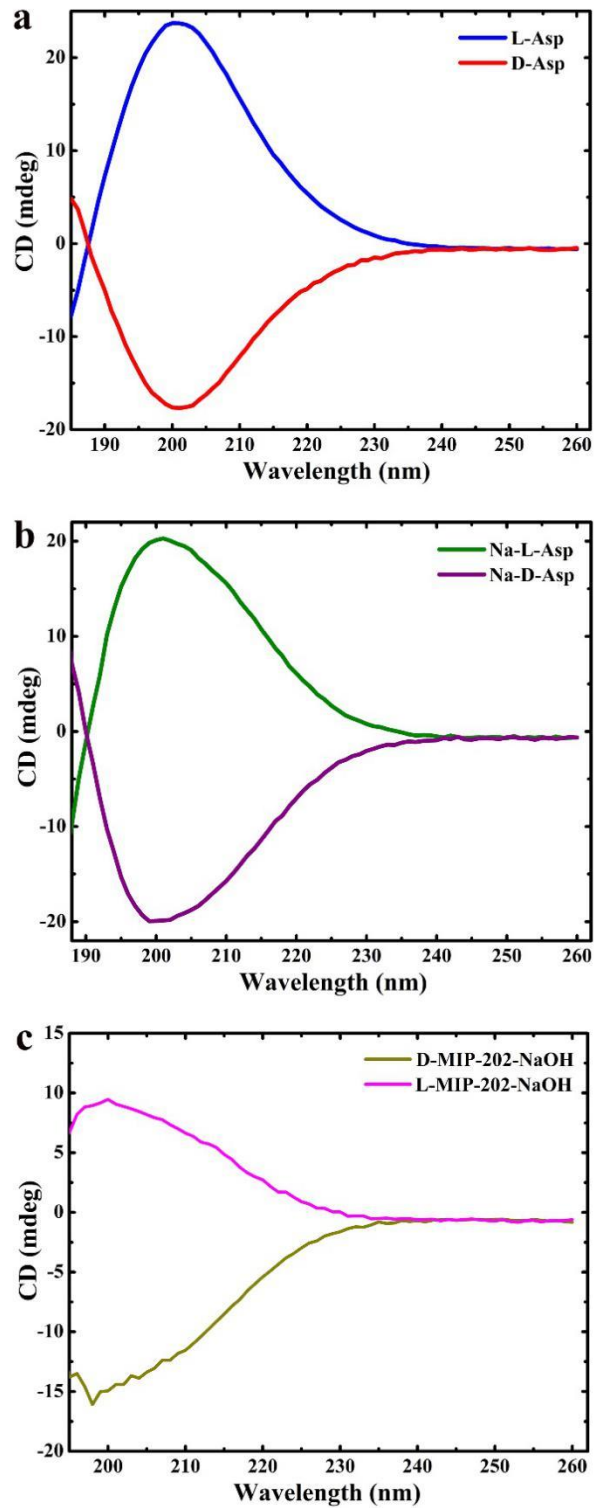
91

92

93

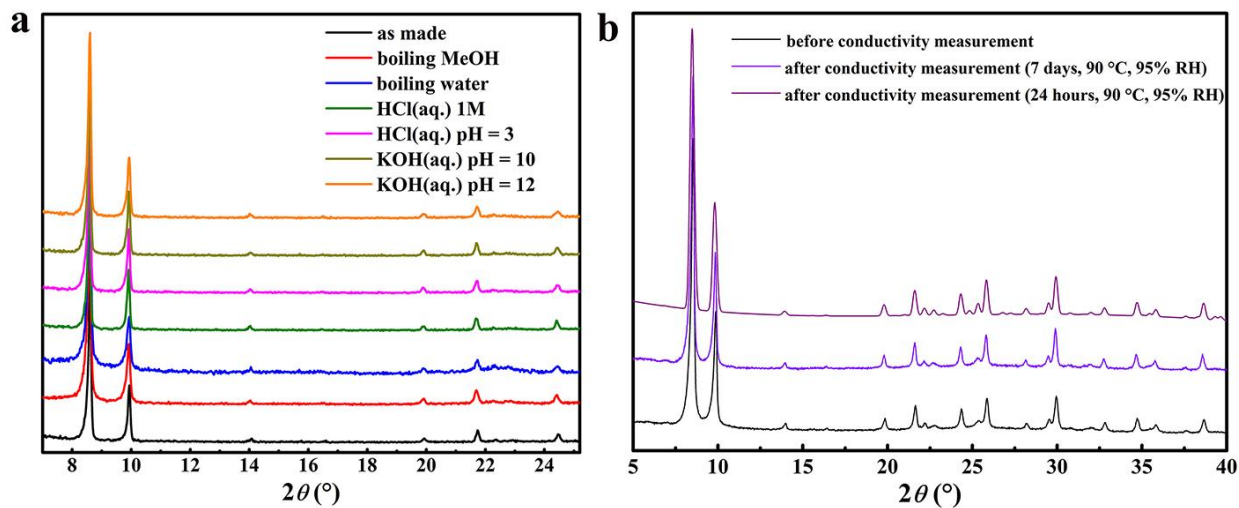
94





95

96 **Supplementary Figure 9.** Circular dichroism (CD) spectra of (a) pure L- and D-aspartic acid in aqueous solution;  
 97 (b) sodium salts of pure L- and D-aspartate in aqueous solution; (c) Aqueous solution of MIP-202(Zr) samples  
 98 digested in NaOH solution.



100 **Supplementary Figure 10.** PXRD pattern comparison of MIP-202(Zr) samples (a) before and after various  
 101 chemical treatments; (b) before and after proton conductivity measurement for different durations.

102

103

104

105

106

107

108

109

110

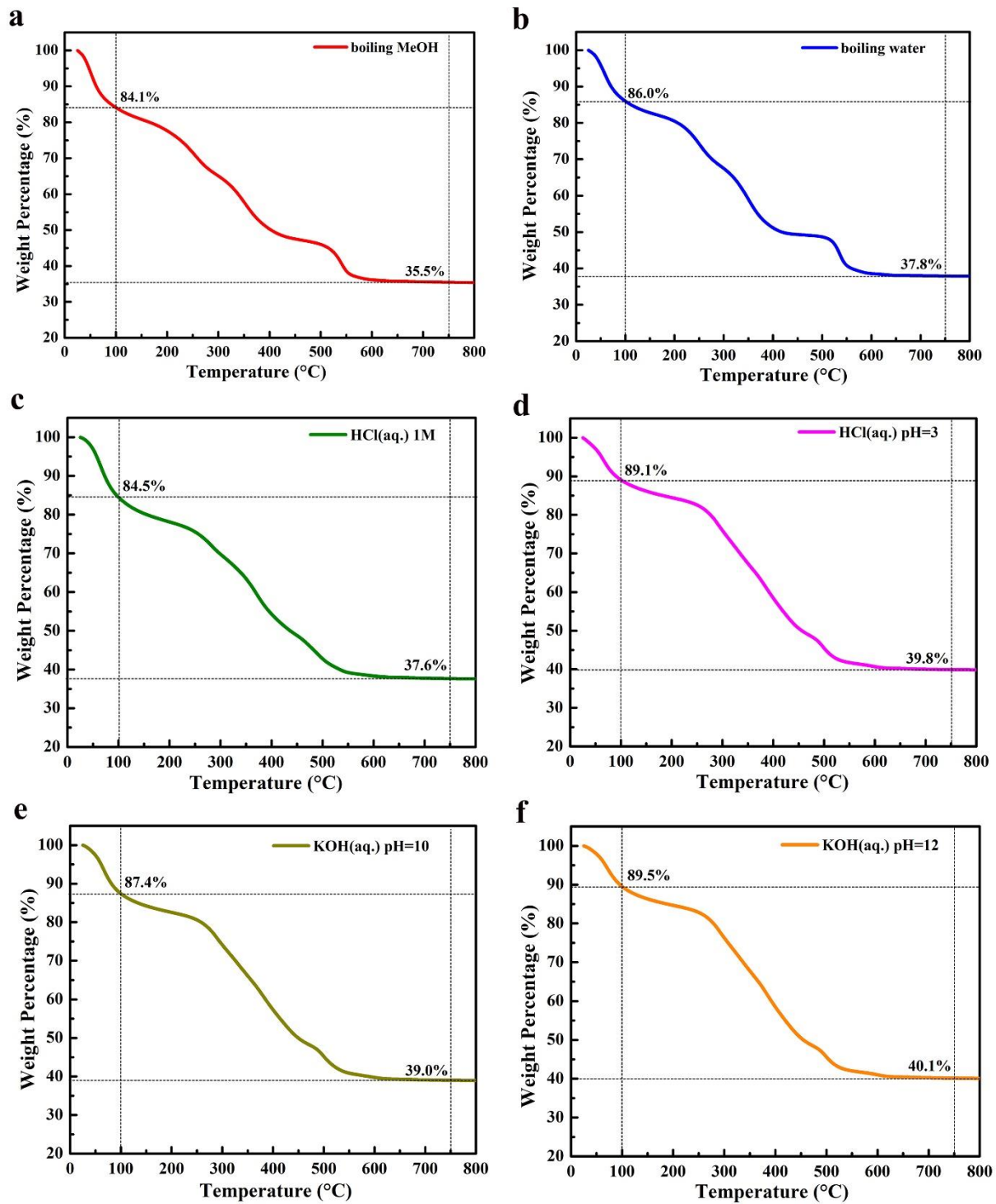
111

112

113

114

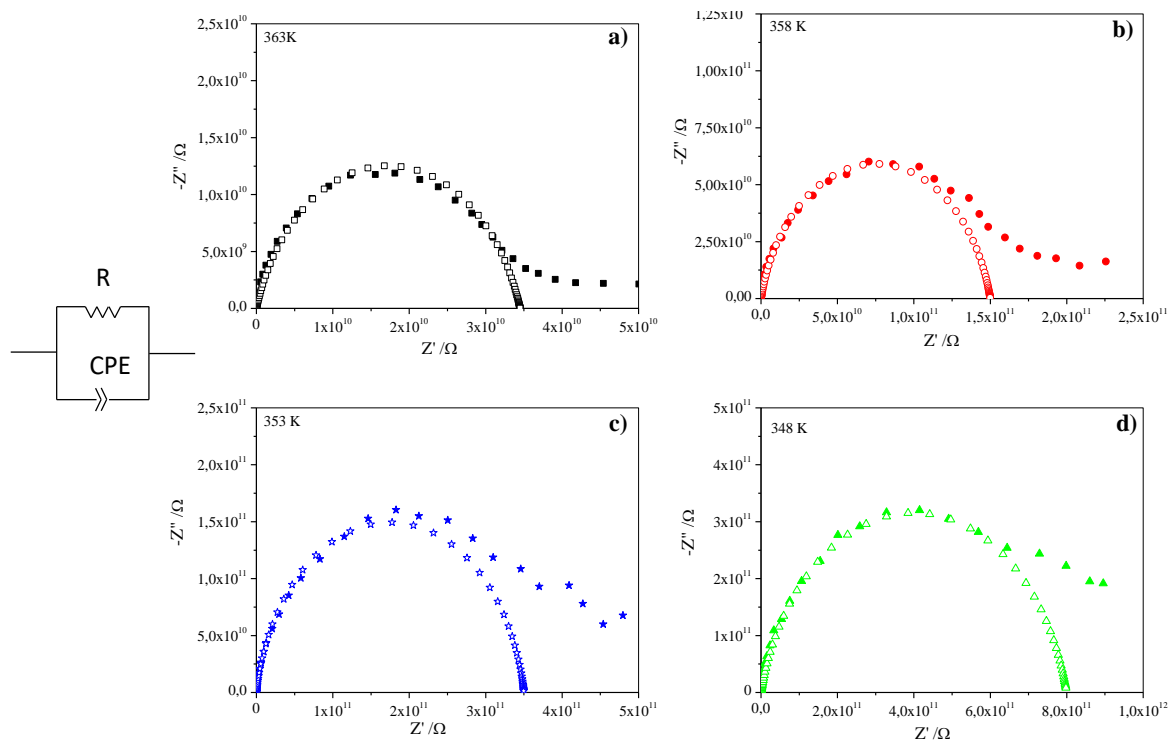
115



116

117 **Supplementary Figure 11.** TGA comparison of MIP-202(Zr) samples after various chemical treatments.

118



119

120 **Supplementary Figure 12.** Nyquist plots of the impedance of the anhydrous MIP-202(Zr) measured at RH = 0%  
 121 and T = a) 363 K b) 358 K c) 353 K and d) 348 K. The filled symbols are the measured impedance data and the  
 122 empty symbols correspond to the fits of the data using the equivalent circuit model detailed on the left.

123

124

125

126

127

128

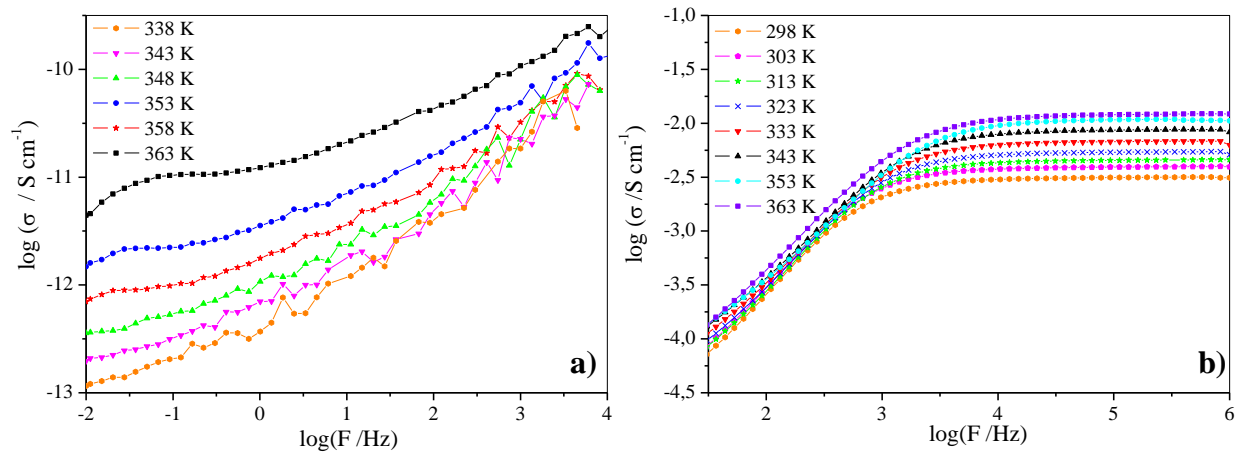
129

130

131

132

133



134

135 **Supplementary Figure 13.** Bode representation of the conductivity versus the frequency in the logarithm scale for

136 (a) the anhydrous and (b) the hydrated MIP-202(Zr).

137

138

139

140

141

142

143

144

145

146

147

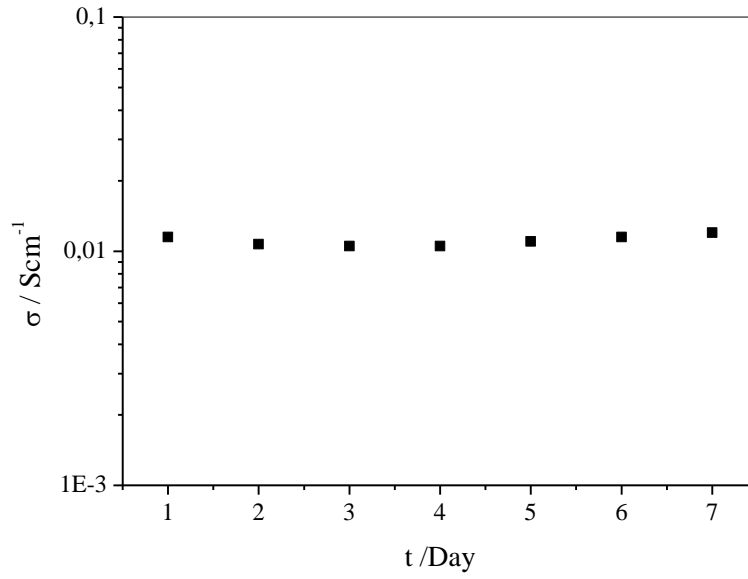
148

149

150

151

152



153

154 **Supplementary Figure 14.** Conductivity of MIP-202(Zr) recorded at 363 K and 95% RH over 7 days.

155

156

157

158

159

160

161

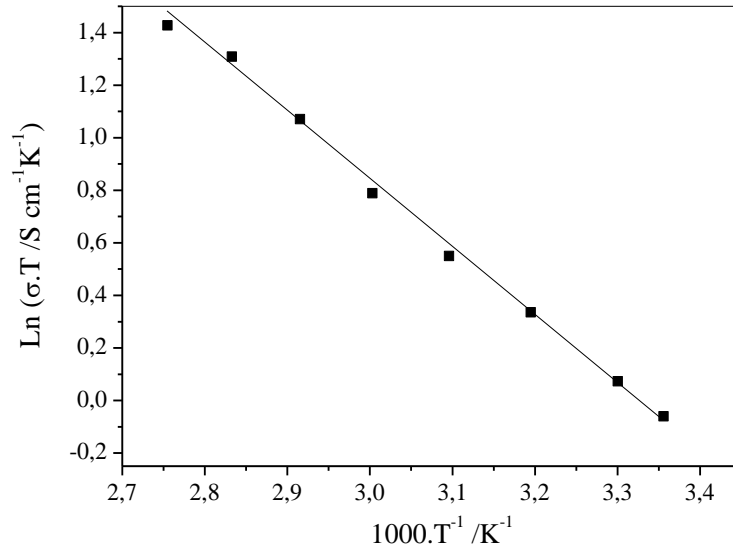
162

163

164

165

166



167

168 **Supplementary Figure 15.** Corresponding Arrhenius plot of the conductivity recorded at 95 % RH for the MIP-  
169 202(Zr). The line corresponds to the linear least-square fit.

170

171

172

173

174

175

176

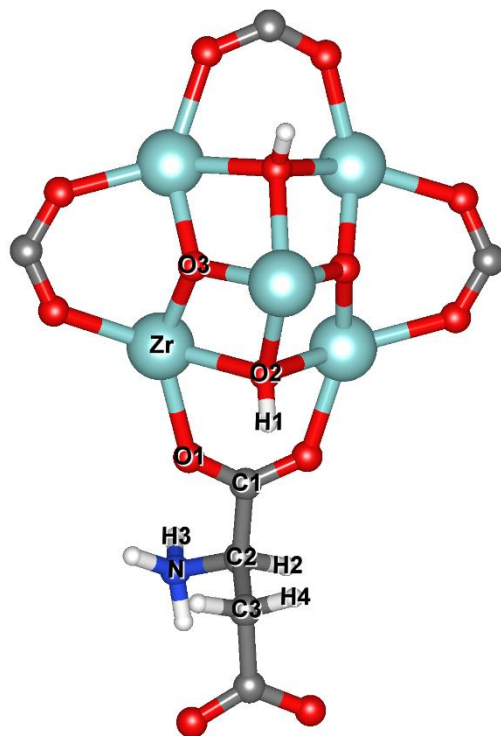
177

178

179

180

181



182

183 **Supplementary Figure 16** Cluster model represents the atom types in MIP-202(Zr), for which the atomic partial  
184 charges are deduced and employed in the MC simulations.

185

186

187

188

189

190

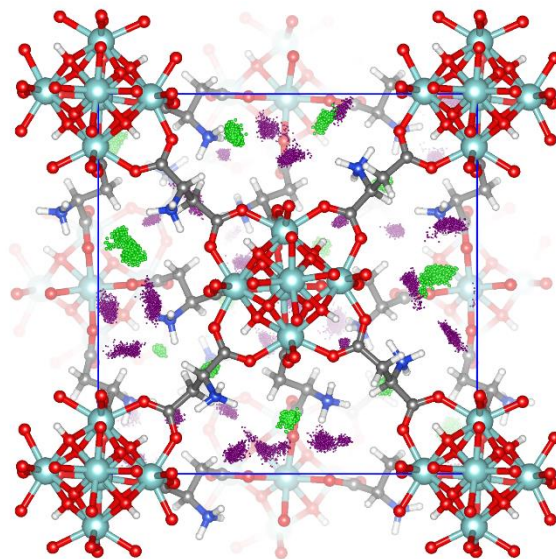
191

192

193

194





195

196 **Supplementary Figure 17** Distribution of the adsorbed water molecules (purple dots) and Cl<sup>-</sup> ions (green dots) in

197 MIP-202(Zr) averaged over the MC steps calculated at 363 K.

198

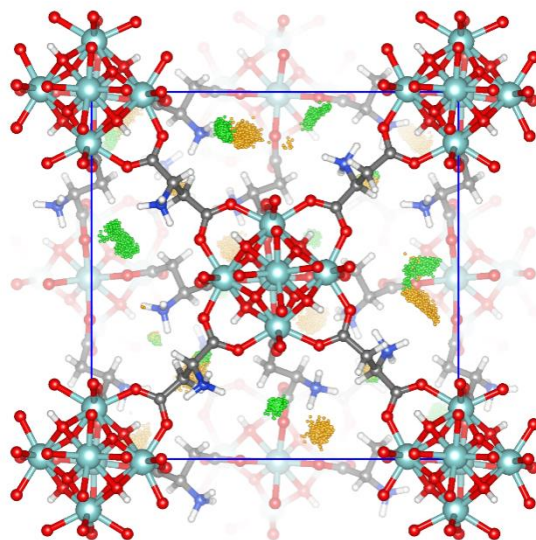
199

200

201

202

203

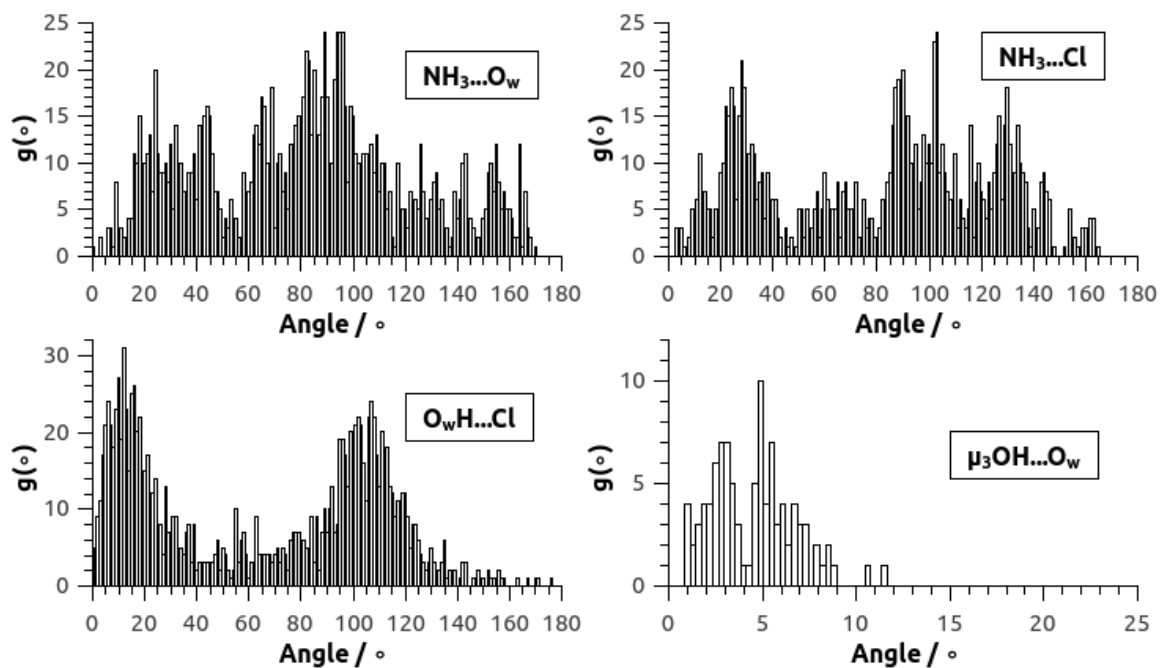


204

205 **Supplementary Figure 18** Comparison of the distributions of Cl<sup>-</sup> ions in anhydrous (gold dots) and hydrated phase  
206 (green dots) in MIP-202(Zr) averaged over the MC steps calculated at 363 K.

207

208



209

210 **Supplementary Figure 19** Distribution of the angles between intramolecular donor-proton vector and the  
 211 intermolecular donor-acceptor vector when the donor-acceptor distances are less than 3.5 Å; averaged over the MC  
 212 configurations generated for the hydrated MIP-202(Zr).

213

214

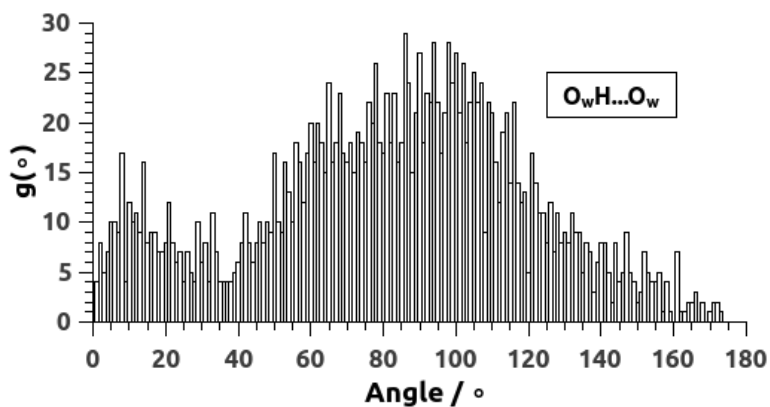
215

216

217

218

219



220

221 **Supplementary Figure 20** Distribution of the angles between the intramolecular O-H vector and the intermolecular

222 O-O vector when the O-O distances of the adsorbed water molecules are less than 3.5 Å; averaged over the MC

223 configurations generated for the hydrated MIP-202(Zr).

224

225

226

227

228

229

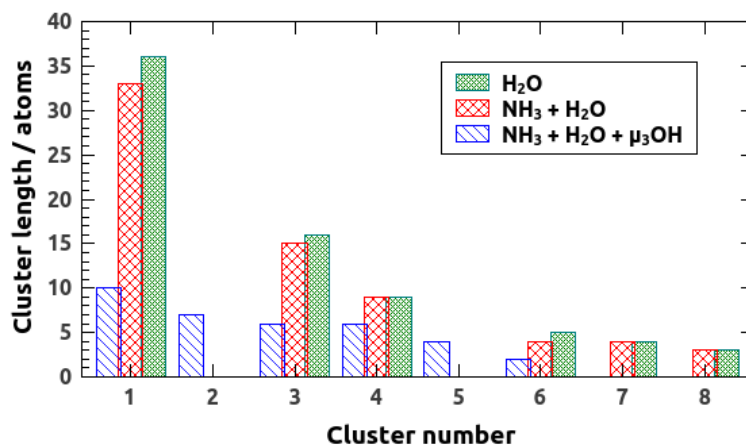
230

231

232

233

234



235  
 236 **Supplementary Figure 21** Size distribution of clusters that aggregates different donor and acceptor atoms,  
 237 calculated solely based on the donor-acceptor distance.  
 238 We aimed to perform quantitative analysis for the clustering of water molecules within the pores  
 239 of MIP-202(Zr) based on the definition of a cluster as a continuous network of water molecules  
 240 interconnected by hydrogen bonds among themselves. The criteria to define the aggregation of the  
 241 water molecules in clusters were the threshold connectivity distance and the aforementioned angle  
 242 between the intramolecular O-H vector and the intermolecular O-O vector. The former was defined  
 243 as 3.2 to accurately represent the first interaction peak of the O-O RDF on liquid water; the latter  
 244 was kept to 37°.

245

246

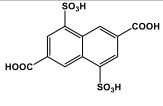
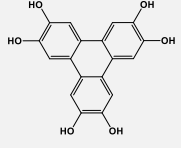
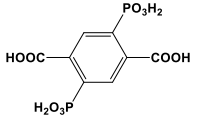
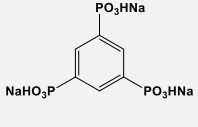
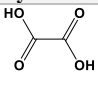
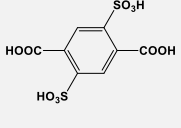
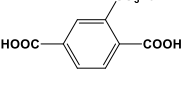

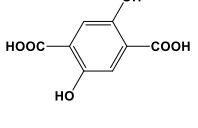
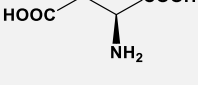
247

248

249

250

251 **Supplementary Table 1.** Comparison of linker availability and MOF preparation condition of reported highly  
 252 proton conductive MOF ( $\geq 10^{-2}$  S cm $^{-1}$ ).

Material	Linker	Reaction Condition
<b>BUT-8(Cr)</b>	 <p>synthetic</p>	solvothermal 190 °C/24 h
<b>Fe-CAT-5</b>	 <p>commercial 1 g/92 € (TCI)</p>	solvothermal 180 °C/48 h
<b>PCMOF10</b>	 <p>synthetic</p>	solvothermal 150 °C/72 h
<b>PCMOF2<sup>1/2</sup></b>	 <p>synthetic</p>	solvothermal 120 °C/48 h
<b>[(Me<sub>2</sub>NH<sub>2</sub>)<sub>3</sub>(SO<sub>4</sub>)<sub>2</sub>][(Zn<sub>2</sub>(ox)<sub>3</sub>]</b>	 <p>commercial 50 g/53.1 € (Sigma)</p>	solvothermal 160 °C/96 h
<b>UIO-66-(SO<sub>3</sub>H)<sub>2</sub></b>	 <p>synthetic</p>	1) Microwave 120 °C/40 min 2) RT oxidation
<b>MIL-101-SO<sub>3</sub>H</b>	 <p>commercial 25 g/101 € (TCI)</p>	solvothermal 190 °C/24 h
<b>TfOH@MIL-101</b>	 <p>commercial 500 g/31 € (Sigma)</p>	1) hydrothermal 220 °C/6 h 2) RT soaking
<b>H<sub>2</sub>SO<sub>4</sub>@MIL-101</b>		
<b>H<sub>3</sub>PO<sub>4</sub>@MIL-101</b>		
<b>H<sup>+</sup>@Ni<sub>2</sub>(dobdc)(H<sub>2</sub>O)<sub>2</sub></b>	 <p>commercial 5 g/78 € (TCI)</p>	1) microwave 110 °C/15 min 2) RT soaking
<b>MIP-202(Zr)</b>	 <p>commercial 1 kg/67 € (Fisher)</p>	reflux in water 1 h/atm.

253

254 **Supplementary Table 2.** SEM-EDX results of MIP-202(Zr) samples.

<b>Treatment</b>	<b>Cl/Zr ratio (atomic)</b>
<b>none</b>	54/46
<b>Reflux in EtOH</b>	51/49
<b>Reflux in MeOH</b>	51/49
<b>Reflux in water once</b>	49/51
<b>Soxhlet extraction with water</b>	31/69
<b>HCl 1M RT</b>	55/45
<b>HCl pH=3 RT</b>	50/50
<b>KOH pH=10 RT</b>	42/58
<b>KOH pH=12 RT</b>	42/58

255

256

257

258

259

260

261

262

263

264

265

266

267 **Supplementary Table 3.** Calculated formulas of MIP-202(Zr) samples after different chemical treatments from  
 268 EDX and TGA results.

	<b>Calculated formula</b>	<b>Missing linker defect</b>
<b>Boiling MeOH</b>	$[\text{Zr}_6\text{O}_4(\text{OH})_4(\text{Aspartate})_6(\text{HCl})_{6.24}] \cdot 18\text{H}_2\text{O}$	-
<b>Boiling water</b>	$[\text{Zr}_6\text{O}_4(\text{OH})_4(\text{Aspartate})_{5.76}(\text{HCl})_{5.76}(\text{OH})_{0.48}(\text{H}_2\text{O})_{0.48}] \cdot 15\text{H}_2\text{O}$	4%
<b>HCl 1M RT</b>	$[\text{Zr}_6\text{O}_4(\text{OH})_4(\text{Aspartate})_{5.42}(\text{HCl})_{7.33}(\text{OH})_{1.16}(\text{H}_2\text{O})_{1.16}] \cdot 17\text{H}_2\text{O}$	10%
<b>HCl pH=3 RT</b>	$[\text{Zr}_6\text{O}_4(\text{OH})_4(\text{Aspartate})_{5.59}(\text{HCl})_6(\text{OH})_{0.82}(\text{H}_2\text{O})_{0.82}] \cdot 11\text{H}_2\text{O}$	7%
<b>KOH pH=10 RT</b>	$[\text{Zr}_6\text{O}_4(\text{OH})_4(\text{Aspartate})_{5.87}(\text{HCl})_{4.34}(\text{OH})_{0.26}(\text{H}_2\text{O})_{0.26}] \cdot 13\text{H}_2\text{O}$	2%
<b>KOH pH=12 RT</b>	$[\text{Zr}_6\text{O}_4(\text{OH})_4(\text{Aspartate})_{5.84}(\text{HCl})_{4.34}(\text{OH})_{0.32}(\text{H}_2\text{O})_{0.32}] \cdot 11\text{H}_2\text{O}$	3%

269

270

271

272

273

274

275

276

277

278

279

280



281 **Supplementary Table 4.** Elemental analysis results of MIP-202(Zr) samples after different chemical treatments.

	Calculated			Found		
	N%	C%	H%	N%	C%	H%
<b>Boiling MeOH</b>	4.16	14.28	3.78	3.61	14.74	4.20
<b>Boiling Water</b>	4.18	14.33	3.62	3.64	13.61	4.07
<b>HCl 1M RT</b>	3.79	12.99	3.79	3.07	12.05	4.30
<b>HCl pH=3 RT</b>	4.21	14.45	3.36	3.78	13.31	3.77
<b>KOH pH=10 RT</b>	4.44	15.23	3.48	3.59	13.66	4.04
<b>KOH pH=12 RT</b>	4.51	15.47	3.34	3.70	13.20	3.89

282

283

284

285

286

287

288

289

290

291

292

293

**Supplementary Table 5.** Conductivity of the anhydrous MIP-202(Zr) recorded at 0% RH.

T/K	Conductivity Bode representation $/S\ cm^{-1}$	Conductivity Nyquist representation $/S\ cm^{-1}$
348	$3.8 \times 10^{-13}$	$4.1 \times 10^{-13}$
353	$9.1 \times 10^{-13}$	$9.5 \times 10^{-13}$
358	$2.2 \times 10^{-12}$	$2.2 \times 10^{-12}$
363	$1.0 \times 10^{-11}$	$9.5 \times 10^{-12}$

294

295

296

297

298

299

300

301

302

303

304

305

**Supplementary Table 6.** Conductivity of MIP-202(Zr) recorded at 95% RH.

T/K	Conductivity	
	Bode representation	Nyquist representation
	$\text{/S cm}^{-1}$	$\text{/S cm}^{-1}$
298	$2.9 \times 10^{-3}$	$2.8 \times 10^{-3}$
303	$3.6 \times 10^{-3}$	$3.2 \times 10^{-3}$
313	$4.5 \times 10^{-3}$	$4.0 \times 10^{-3}$
323	$5.4 \times 10^{-3}$	$4.7 \times 10^{-3}$
333	$6.6 \times 10^{-3}$	$6.0 \times 10^{-3}$
343	$8.5 \times 10^{-3}$	$7.5 \times 10^{-3}$
353	$1.0 \times 10^{-2}$	$1.0 \times 10^{-2}$
363	$1.1 \times 10^{-2}$	$1.1 \times 10^{-2}$

306

307

308

309

310

311

312

313

314

315

316 **Supplementary Table 7** Atomic partial charges of MIP-202(Zr) atom types.

<b>Atom type</b>	<b>Charge (e)</b>
<b>H1</b>	0.365
<b>H2</b>	0.205
<b>H3</b>	0.300
<b>H4</b>	0.183
<b>C1</b>	0.574
<b>C2</b>	-0.158
<b>C3</b>	-0.285
<b>N</b>	-0.295
<b>O1</b>	-0.552
<b>O2</b>	-0.798
<b>O3</b>	-1.031
<b>Cl</b>	-0.700
<b>Zr</b>	2.003

317

318

319

320

321

322

323

324

325

326

327

328

329 **Supplementary Table 8** LJ potential parameters for the atoms of MIP-202(Zr).

Atom type	$\sigma$ (Å)	$\epsilon/k_B$ (K)
Zr	2.783	34.722
O	3.118	30.193
C	3.473	47.857
N	3.263	38.949
Cl	3.516	114.232
H	2.846	7.649

330

331

332

333

334

335

336

337

338

339

340

341

342 **Supplementary Table 9.** LJ Potential parameters and partial charges for the adsorbate molecules

Atom type	$\sigma$ (Å)	$\epsilon/k_B$ (K)	$q$ ( $e$ )
O_e	3.1589	93.200	0.0000
H_e	0.00	0.000	0.5564
M_e	0.00	0.000	-1.1128
N2_N	3.310	36.000	-0.4820
N2_COM	0.00	0.000	0.9640

343

344

345

346

347

348

349

350

351

352

353

354

355

## 356 **Supplementary Note 1**

### 357 **Structure solution**

358 The crystal structure of MIP-202 was solved using our newly developed software based on the  
359 AASBU strategy we described elsewhere. The geometry optimizations at the DFT level were  
360 performed using the Quickstep module<sup>1</sup> of the CP2K program<sup>2,3</sup> employing the Gaussian Plane  
361 Wave (GPW) formalism. The general gradient approximation (GGA) to the exchange-correlation  
362 functional according to Perdew-Burke-Ernzerhof (PBE)<sup>4</sup> was used in combination of Grimme's  
363 DFT-D3 semi-empirical dispersion corrections.<sup>5,6</sup> Triple- $\zeta$  plus valence polarized Gaussian-type  
364 basis sets (TZVP-MOLOPT) were considered for all atoms, except for the Zr metal centers, where  
365 double- $\zeta$  plus valence polarization functions (DZVP-MOLOPT) were employed.<sup>7</sup> The interactions  
366 between core electrons and valence shells of the atoms were described by the pseudopotentials  
367 derived by Goedecker, Teter, and Hutter (GTH).<sup>8-10</sup> The auxiliary plane wave basis sets were  
368 truncated at 400 Ry.

### 369 **Monte Carlo simulations**

370 The MC calculations were performed in the NVT ensemble at 90 °C with a simulation box of 8  
371 conventional unit cells ( $2 \times 2 \times 2$ ) containing 24  $\text{Cl}^-$  and loaded with 51  $\text{H}_2\text{O}$  molecules per unit  
372 cell as determined by the thermogravimetric analysis. The interactions between the guest water  
373 molecules and the MOF structure were described by a combination of site-to-site Lennard-Jones  
374 (LJ) contributions and Coulombic terms. A mixed set of universal force field (UFF)<sup>11</sup> and  
375 DREIDING force field<sup>12</sup> parameters were adopted to describe the LJ parameters for the atoms in  
376 the inorganic and organic part of the framework. The water molecules were described by the  
377 TIP4P/2005 potential model<sup>13</sup> corresponding to a microscopic representation of four LJ sites.  
378 Following the treatment adopted in other well-known force fields,<sup>14,15</sup> the hydrogen atoms of the

379 hydroxyl ( $\mu_3\text{OH}$  group of inorganic nodes) and  $\text{NH}_3$  functional groups (in the aspartic acid ligands)  
380 interact with the adsorbate water molecules only via the Coulombic potential, consistent with the  
381 strategy we validated in previous studies.<sup>16,17</sup> Short-range dispersion forces were truncated at a  
382 cutoff radius of 12 Å while the interactions between unlike force field centers were treated by  
383 means of the Lorentz-Berthelot combination rule. The long-range electrostatic interactions were  
384 handled using the Ewald summation technique. Hence,  $2 \times 10^8$  Monte Carlo steps have been used  
385 for both equilibration and production runs. These MC calculations were performed using the  
386 Complex Adsorption and Diffusion Simulation Suite (CADSS) code.<sup>18</sup> To gain insight into the  
387 arrangement of the water guests in MIP-202, the guest–guest and guest–host radial distribution  
388 functions (RDFs), the density probability distributions for all of the guests and  $\text{Cl}^-$  ions, and the  
389 number of hydrogen bonds, size of the water clusters were calculated by averaging over hundreds  
390 of configurations generated during the MC simulations.

### 391 **Atomic partial charge calculations**

392 Single point energy calculations and Mulliken population analysis<sup>19</sup> were performed to extract the  
393 partial charges for each atom type of the MIP-202(Zr) framework using DMol3 code. These  
394 calculations were based on the PBE functional and the double numerical basis set containing  
395 polarization functions (DNP).<sup>20</sup>

### 396 **Pore size distribution calculations**

397 The methodology reported by Gelb and Gubbins<sup>21</sup> was used to calculate the pore size distributions  
398 (PSD) of the MIP-202 structures, as shown in Supplementary Figure 6. In these calculations, the  
399 van der waals parameters of the framework atoms were adopted from the DREIDING<sup>12</sup> force  
400 field except for Zr atom, for which the parameters were taken from the universal force field (UFF)<sup>11</sup>  
401 as they are not available in the former.



402 **Supplementary Note 2**

403 The data collection and refinement parameters of MIP-202(Zr) single crystal structure are  
404 indicated as following:

405

406 *Crystal data*

407  $C_{24}H_{42}N_6O_{32}Zr_6$

$D_x = 1.728 \text{ g.cm}^{-3}$

408  $Mr = 1473.95 \text{ g.mol}^{-1}$

Synchrotron radiation,  $\lambda = 0.70846 \text{ \AA}$

409 Cubic,  $Pn-3$

$\mu = 1.13 \text{ mm}^{-1}$

410  $a = 17.826 (2) \text{ \AA}$

$T = 100 \text{ K}$

411  $V = 5665 (2) \text{ \AA}^3$

Needle, colorless

412  $Z = 4$

$0.03 \times 0.01 \times 0.01 \text{ mm}$

413  $F(000) = 2896$

414

415 *Data collection*

416 PROXIMA 2A - Synchrotron SOLEIL

1509 reflections with  $I > 2\sigma(I)$

417 diffractometer

$R_{int} = 0.170$

418 Radiation source: synchrotron

$\theta_{max} = 24.7^\circ$ ,  $\theta_{min} = 1.6^\circ$

419  $\varphi$  scan

$h = -20 \rightarrow 19$

420 36542 measured reflections

$k = -20 \rightarrow 20$

421 1627 independent reflections

$l = -20 \rightarrow 20$

422

423 *Refinement*

424 Refinement on  $F^2$

Hydrogen site location: inferred from  
neighbouring sites

425 Least-squares matrix: full

H-atom parameters constrained

426  $R[F^2 > 2\sigma(F^2)] = 0.140$

$w = 1/[\sigma^2(F_o^2) + (0.1172P)^2 + 197.4568P]$

427  $wR(F^2) = 0.352$

where  $P = (F_o^2 + 2F_c^2)/3$

428  $S = 1.15$

$(\Delta/\sigma)_{max} = 0.007$

429 1627 reflections

$\Delta\rho_{max} = 2.63 \text{ e.\AA}^{-3}$

430 91 parameters

$\Delta\rho_{min} = -4.17 \text{ e.\AA}^{-3}$

431 23 restraints

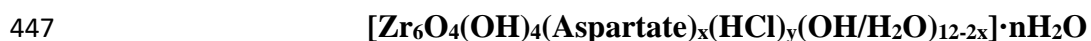
432

### 433 **Supplementary Note 3**

#### 434 **Combined analysis of EDX, TGA and elemental analysis results**

435 In order to calculate the possible amount of structural defect generation and the corresponding  
436 structure formulas of the samples after different chemical treatments, a combined analysis of EDX,  
437 TGA and elemental analysis results was carried out as below:

438 The ideal formula for the MIP-202(Zr) is  $[\text{Zr}_6\text{O}_4(\text{OH})_4(\text{Aspartate})_6(\text{HCl})_6] \cdot n\text{H}_2\text{O}$ . There are three  
439 possibilities of structural defects generated: 1) missing linker; 2) missing inorganic SBU and 3)  
440 both organic and inorganic moieties are missing. TGA data support that the organic parts are  
441 always less or equal to the ideal ratio for all the samples involved, which excludes the second and  
442 the third possibilities of defects. In this case, only missing linker defect will be taken into  
443 consideration for calculation. When one aspartate linker is missing, there must be two pairs of –  
444 OH/H<sub>2</sub>O to complete the coordination vacancy and balance the charge instead. The amount of  
445 trapped HCl also could be varied along treatments under different conditions. Thus the formula of  
446 the MIP-202(Zr) sample after treatment turns to be:



448 in which y could be calculated from EDX result while x and n could be deduced from TGA data.  
449 Then the calculated CHN percentages obtained from the resulting formula could be compared with  
450 the experimental ones in order to check the accuracy of the aforementioned calculation.

451 For example, the EDX result of the boiling MeOH washed sample is Cl/Zr=51/49 (atomic ratio),  
452 thus y=6.24 in this case (Supplementary Table 2). In the corresponding TGA curve  
453 (Supplementary Fig. 11a), a weight loss of 15.9% before 100 °C was ascribed to the removal of  
454 guest water molecules. The final weight percentage of 35.5% at 800 °C corresponds to the ZrO<sub>2</sub>

455 residue after burning the MOF sample in oxygen. Thus a weight loss of 48.6% was signed to the  
456 decomposition of the MOF and releasing the organic part. Thereby, the sample formula was  
457 calculated to be  $[\text{Zr}_6\text{O}_4(\text{OH})_4(\text{Aspartate})_6(\text{HCl})_{6.24}] \cdot 18\text{H}_2\text{O}$ . The calculated CHN percentages from  
458 this formula are C 14.28%, H 3.78% and N 4.16%, in a good agreement with the experimental data  
459 (C 14.74%, H 4.20% and N 3.61%).

460 The same calculation was carried out for all the samples tested and their corresponding formulas  
461 are listed in Supplementary Table 3. In general, the calculated CHN percentages are in an  
462 acceptable error range in comparison with the experimental ones, suggesting that those calculated  
463 formulas are reasonable. Refluxing the pristine MIP-202(Zr) sample in water generates 4% of  
464 missing linker defect. Acid treatments result in increased amount of missing linker defect. Weak  
465 bases play an important role in removing trapped HCl molecules rather than making missing linker  
466 defect. Therefore, the presence of structural defect and removal of trapped HCl could be  
467 responsible for the increased uptakes in their corresponding nitrogen adsorption isotherms when  
468 compared with that of the pristine sample.

469

470

471

472

473

474

475

## 476 **Supplementary Note 4**

### 477 **AC impedance measurements**

#### 478 **Bode and Nyquist representations**

479 In the Bode diagram, the real part of the measured *ac* conductivity ( $\sigma_{ac}(\omega, T)$ ) typically results from  
480 the superposition of three contributions: the Maxwell Wagner Sillars response  $\sigma_{MWS}(\omega, T)$ , the  
481 diffusion conductivity  $\sigma_{dc}(T)$  and the polarization conductivity  $\sigma_{pol}(\omega, T)$  (**Equation 1**):

$$482 \quad \sigma_{ac}(\omega, T) = \sigma_{MWS}(\omega, T) + \sigma_{dc}(T) + \sigma_{pol}(\omega, T), \quad (1)$$

483 where  $\omega$  is the electrical field angular frequency and  $T$  is the temperature. The diffusion  
484 conductivity corresponds to long-range redistribution of charges, i.e. ionic or electron transport,  
485 while the polarization contribution arises from local rearrangement of charges or dipoles causing  
486 dipolar reorientation and thus resulting in the intrinsic bulk polarization. Maxwell Wagner Sillars  
487 (MWS) polarization is due to the accumulation of charges at the sample/electrodes interface and  
488 also depends on extrinsic parameters, such as the sample shape.

489 The Bode plots of the anhydrous and hydrated MIP-202(Zr) recorded at 363 K are illustrated in  
490 Supplementary Figs. 13a and 13b, respectively. The conductivity profiles of both solids are in  
491 sharp contrast, evidencing the water-mediated proton conductor behavior of MIP-202(Zr). The  
492 anhydrous material response is mainly dominated by the conductivity increase with frequency  
493 corresponding to the polarization contribution, associated with the local rearrangements of  $\text{NH}_3^+$   
494 and/or  $\text{Cl}^-$  species. The low frequency conductivity plateau due to the long-range displacement of  
495 charges is only observable for the higher temperature range, with values corresponding to that of  
496 an insulator ( $\sigma < 10^{-11} \text{ S.cm}^{-1}$ , Supplementary Table 5). The signal decrease at very low frequency  
497 illustrates the Maxwell Wagner Sillars response due to the accumulation of charges at the

498 sample/electrodes interface and consequently indicates the ionic features of the conductivity.  
499 Being opposite, the conductivity recorded at 95% RH is drastically different: the apparent  
500 conductivity plateau is centered around  $10^{-3}$ - $10^{-2}$  S.cm<sup>-1</sup> (Supplementary Table 6) and is  
501 accompanied by the Maxwell Wagner Sillars response responsible for the conductivity falling at  
502 lower frequency, whereas the polarization contribution is no more observable in the so-studied  
503 frequency range.

504 For comparison, the Nyquist plot of the anhydrous and hydrated MIP-202(Zr) were also considered.  
505 The bulk resistance was deduced directly from the impedance plot extrapolation in the case of the  
506 hydrated sample or from the fitting of the Nyquist plot using equivalent circuit models for the  
507 anhydrous material (Supplementary Fig. 12). Conductivity ( $\sigma$ /S.cm<sup>-1</sup>) was calculated considering  
508  $\sigma = 1/R \times l/S$ , where  $l$  and  $S$  are the sample thickness (cm) and surface (cm<sup>2</sup>), respectively, and  
509  $R$  is the bulk resistance of the sample ( $\Omega$ ).

510 Conductivity values deduced from the Bode diagram and the Nyquist representation are  
511 comparable (Supplementary Tables 5 and 6), supporting that both methods can be equally  
512 considered.

513

514

515

516

517

518 **References**

- 519 1 J. VandeVondele, M. Krack, F. Mohamed, M. Parrinello, T. Chassaing and J. Hutter, *Comput.*  
520 *Phys. Commun.*, 2005, **167**, 103–128.
- 521 2 J. Hutter, M. Iannuzzi, F. Schiffmann and J. VandeVondele, *Wiley Interdiscip. Rev. Comput. Mol.*  
522 *Sci.*, 2014, **4**, 15–25.
- 523 3 The CP2K developers group, <http://www.cp2k.org>.
- 524 4 J. P. Perdew, K. Burke and M. Ernzerhof, *Phys. Rev. Lett.*, 1996, **77**, 3865–3868.
- 525 5 S. Grimme, J. Antony, S. Ehrlich and H. Krieg, *J. Chem. Phys.*, 2010, **132**, 154104.
- 526 6 S. Grimme, *J. Comput. Chem.*, 2004, **25**, 1463–73.
- 527 7 J. VandeVondele and J. Hutter, *J. Chem. Phys.*, 2007, **127**, 114105.
- 528 8 S. Goedecker, M. Teter and J. Hutter, *Phys. Rev. B*, 1996, **54**, 1703–1710.
- 529 9 M. Krack, *Theor. Chem. Acc.*, 2005, **114**, 145–152.
- 530 10 C. Hartwigsen, S. Goedecker and J. Hutter, *Phys. Rev. B*, 1998, **58**, 3641–3662.
- 531 11 a. K. Rappe, C. J. Casewit, K. S. Colwell, W. a. Goddard and W. M. Skiff, *J. Am. Chem. Soc.*,  
532 1992, **114**, 10024–10035.
- 533 12 S. L. Mayo, B. D. Olafson and W. A. Goddard, *J. Phys. Chem.*, 1990, **94**, 8897–8909.
- 534 13 J. L. F. Abascal and C. Vega, *J. Chem. Phys.*, 2005, **123**, 234505.
- 535 14 C. D. Wick, M. G. Martin and J. I. Siepmann, *J. Phys. Chem. B*, 2000, **104**, 8008–8016.
- 536 15 W. L. Jorgensen, D. S. Maxwell and J. Tirado-Rives, *J. Am. Chem. Soc.*, 1996, **118**, 11225–11236.
- 537 16 Q. Yang, S. Vaesen, F. Ragon, A. D. Wiersum, D. Wu, A. Lago, T. Devic, C. Martineau, F.

- 538 Taulelle, P. L. Llewellyn, H. Jobic, C. Zhong, C. Serre, G. De Weireld and G. Maurin, *Angew.*  
539 *Chemie Int. Ed.*, 2013, **52**, 10316–10320.
- 540 17 A. Cadiau, J. S. Lee, D. Damasceno Borges, P. Fabry, T. Devic, M. T. Wharmby, C. Martineau, D.  
541 Foucher, F. Taulelle, C.-H. Jun, Y. K. Hwang, N. Stock, M. F. De Lange, F. Kapteijn, J. Gascon,  
542 G. Maurin, J.-S. Chang and C. Serre, *Adv. Mater.*, 2015, **27**, 4775–4780.
- 543 18 Q. Yang and C. Zhong, *J. Phys. Chem. B*, 2006, **110**, 17776–17783.
- 544 19 R. S. Mulliken, *J. Chem. Phys.*, 1955, **23**, 1833–1840.
- 545 20 W. J. Hehre, R. Ditchfield and J. A. Pople, *J. Chem. Phys.*, 1972, **56**, 2257–2261.
- 546 21 L. D. Gelb and K. E. Gubbins, *Langmuir*, 1999, **15**, 305–308.

547

548

549

550

551